frontiers | Frontiers in Physics

TYPE Original Research
PUBLISHED 05 March 2024
DOI 10.3389/fphy.2024.1331133



OPEN ACCESS

EDITED BY
Bożena Jarząbek,
Polish Academy of Sciences, Poland

REVIEWED BY
R. C. Singh,
Sharda University, India
Paweł Gnida,
Polish Academy of Sciences, Poland

*CORRESPONDENCE
Kamal A. Aly,
kaali5@uj.edu.sa

RECEIVED 31 October 2023
ACCEPTED 08 February 2024
PUBLISHED 05 March 2024

CITATION
Aly KA, Ismail YAM, Salman S. Alsulami Z, Abolibda TZ, Almohammedi A, Gomha SM, Ahmed HA and Ibrahim MS (2024), Effect of Sn nanoparticles on the optical properties of PEDOT:PSS thin films.
*Front. Phys.* 12:1331133.
doi: 10.3389/fphy.2024.1331133



# Effect of Sn nanoparticles on the optical properties of PEDOT:PSS thin films

Kamal A. Aly[1,2]*, Yasser A. M. Ismail[3], Ziad Salman S. Alsulami[3], Tariq Z. Abolibda[4], Abdullah Almohammedi[3], Sobhi M. Gomha[4], Hoda A. Ahmed[5,6] and Mohamed S. Ibrahim[3]

[1]Department of Physics, Collage of Science and Arts, Jeddah University, Jeddah, Saudi Arabia, [2]Department of Physics, Faculty of Science, Al-Azhar University, Asyut, Egypt, [3]Department of Physics, Faculty of Science, Islamic University of Madinah, Madinah, Saudi Arabia, [4]Department of Chemistry, Faculty of Science, Islamic University of Madinah, Madinah, Saudi Arabia, [5]Department of Chemistry, Faculty of Science, Cairo University, Giza, Egypt, [6]Chemistry Department, College of Sciences, Taibah University, Yanbu, Saudi Arabia

**Introduction:** In this study, we focus on enhancing the optical properties of PEDOT:PSS thin films by incorporating pure Sn nanoparticles (NPs) synthesized using the ultrasonic ablation technique. The objective is to investigate the impact of Sn concentration on the optical characteristics of the films, with a specific emphasis on applications in organic solar cells.

**Methods:** We systematically varied the concentrations of Sn in PEDOT:PSS thin films and characterized their optical properties. The index of refraction (n) and extinction coefficient (k) were precisely determined by analyzing the transmission and reflection spectra of the films. Additionally, Sellmeier's dispersal model was employed to elucidate the obtained results of n, and dispersive factors were calculated and interpreted.

**Results:** The incorporation of Sn nanoparticles led to improvements in the energy bandgap (Eg) values of PEDOT:PSS films. Notably, as the concentration of Sn increased, the n values decreased, indicating enhanced suitability for organic solar cell applications. The study also unveiled a decrease in the dielectric constant of PEDOT:PSS/Sn films with increasing Sn content, resulting in improved transmittance velocity and enhanced efficacy of microelectronic devices. This, in turn, promotes the development of large-frequency and large-velocity stretchy circuit boards.

**Discussion:** The comprehensive assessment of optical and dielectric parameters, including complex dielectric constant, complex optical conductance, and nonlinear optical constants, provides valuable insights into the potential applications of PEDOT:PSS/Sn films. The larger nonlinear optical constants observed in the present films suggest their suitability for diverse applications such as all-optical switching, limiting, phase modulation, and frequency conversion. Overall, our findings highlight the promising potential of Sn-incorporated PEDOT:PSS thin films in advancing the field of optoelectronics and microelectronics.

KEYWORDS

**organic solar cells, *Sn* nanoparticles, optical properties of thin films, dielectrics, PEDOT:PSS thin film**

# 1 Introduction

An important layer in different applications is the poly(3,4-ethylenedioxythiophene):poly(styrene sulfonate) (PEDOT:PSS) layer. Water-soluble PEDOT:PSS with different conductance grades can introduce good transparency in the visible region with high work function, low density, low thermal conductance, excellent thermal constancy, respectable compatibility, elasticity, and low production costs, depending on the solution [1]. Using different preparation techniques [2–6], PEDOT:PSS aqueous dispersion can easily be deposited to produce thin films with good uniformity. Otherwise, the PEDOT:PSS layer in several devices can be prepared by several simple and easy techniques at room temperature. Due to its unique properties, PEDOT:PSS is widely used in several applications, *viz.*, different types of solar cells, organic light-emitting diodes, thermoelectric devices, electronic paper, sensors, fuel cells, carbon-capturing membranes, touch panel displays, and supercapacitors [7–14]. In solar cell applications, PEDOT:PSS is commonly used as a gap transporting plate or an electron transporting layer [7–9, 15], which can facilitate transferring charge carriers into specific electrodes.

Unfortunately, PSS moieties in the PEDOT:PSS solution are an insulator part that may deteriorate the electrical conductance of the PEDOT:PSS layer. In addition, the crystal nature of PEDOT moieties is not sufficient to encourage charge carriers to be transported through the PEDOT:PSS layer and collected by electrodes using the optoelectronic devices. Many attempts have been made to increase the electric conductance and optical transmittance of PEDOT:PSS to make them more efficient in optoelectronic devices. Among these attempts was the incorporation of organic compounds, *viz.*, ethylene glycol (EG), methanol, ethanol, sorbitol, dimethyl sulfoxide, dimethylformamide, and fluoride surfactant, into a PEDOT:PSS aqueous solution [16–22]. The chemically functionalized multi-walled carbon nanotubes were added to the PEDOT:PSS solution to enhance the implementation of the parameters of organic solar cells [23]. Unfortunately, all previous organic compounds can impair the chemical structure of the host PEDOT:PSS solution because of the possible collaboration between the host PEDOT:PSS solution and the chemical compounds. Therefore, the physical properties (electrical conductivity and optical transparency) of PEDOT:PSS thin films can fluctuate due to the effectiveness of such chemical compounds.

The modification of the PEDOT:PSS solution by metal nanoparticle (NP) incorporation, *viz.*, Ag, Au, and Al, is an effective approach, for improving the physical properties of PEDOT:PSS films [24]. Notarianni et al. [24] stated that Au NPs, which were introduced using the liquid chemical technique, may be incorporated into the PEDOT:PSS solution, which provides good dispersion and homogeneity in the solution. For increasing the conversion competence of organic solar cells, Woo et al. [25] prepared Au and Ag NPs using the chemical technique in the PEDOT:PSS solution through the reduction of chloroauric acid ($HAuCl_4$) and silver nitrate ($AgNO_3$), respectively, with a sodium borohydride ($NaBH_4$) solution inside of the aqueous PEDOT:PSS solution. Unfortunately, metal NPs synthesized by chemical methods may have traces of the chemicals and some additives that can make a passivation layer or surfactant around the prepared NPs. The presence of such additives and chemical traces in the PEDOT:PSS solution may alter its chemical structure, and consequently, the physical properties of PEDOT:PSS thin films may be changed [26].

The improvement of the physical properties of PEDOT:PSS thin films through the incorporation of metal NPs while evading any type of chemical additions may be achieved by the generation of metal NPs in the same PEDOT:PSS solution with our promising ultrasonic ablation method [26–28], which signifies a top-down physical technique. Within this method, pure metal NPs may be formed by the effect of ultrasonic radiation on metal thin films engaged in the same PEDOT:PSS solution. Therefore, pure metal NPs may be incorporated in the PEDOT:PSS solution, avoiding the surfactants or passivation layers that may be present on the surface of the prepared NPs using chemical methods.

In the current investigation, we attempt to improve the optical parameters of PEDOT:PSS thin films by incorporating pure tin (Sn) NPs prepared using the ultrasonic ablation technique. Through this method, different Sn NP concentrations can be incorporated into the PEDOT:PSS solution, and then, PEDOT:PSS/Sn thin films can be spin coated on clean glass substrates. For determining the optical properties of PEDOT:PSS thin films, without and with different concentrations of Sn NPs, film transmittance ($T$) and reflectance ($R$) were characterized using a Jasco-630 V double-beam spectrometer. Then, different optical constants of PEDOT:PSS/Sn thin films were calculated and discussed.

# 2 Experimental procedures

## 2.1 Materials

Natural Sn shots (99.99% from Kurt J. Lesker Company Ltd., UK) were deposited onto clean glass substrates. The PEDOT:PSS solution (1.3 wt% dispersal in $H_2O$, conductance grade with 1 S/cm conductivity) was purchased from Sigma-Aldrich and used after filtration by using a 0.22-μm PTFE filter.

## 2.2 Fabrication of Sn NPs in the PEDOT:PSS solution using the ultrasonic ablation method

The generation of Sn NPs inside the PEDOT:PSS solution was carried out physically using the ultrasonic ablation technique. In the beginning, a thin film of Sn metal, having a thickness of around 200 nm, was evaporated on a clean glass substrate (1 × 1 $cm^2$) using the thermally evaporating technique (DONG, Korea) at a pressure of ~3.8 × $10^{-7}$ torr. The PEDOT:PSS solution was filtered using a 0.22-μm PTFE filter before being used. The Sn thin film was immersed inside 1 mL of the filtered PEDOT:PSS solution in a clean glass bottle, which was dipped in an ultrasonic bath (VWR, USC-TH, Malaysia) under the effect of a frequency of 45 kHz for 30 min. For an accurate comparison, a pristine PEDOT:PSS solution (without Sn thin film) was sonicated for the same period.

TABLE 1 Mixtures of the PEDOT:PSS/Sn solution with the pristine PEDOT:PSS solution to prepare different Sn NP concentrations incorporated into the PEDOT:PSS solution.

| Sample name | Amount of pristine PEDOT:PSS solution (μL) | Amount of PEDOT:PSS/Sn solution (μL) | Vol% of the PEDOT:PSS/Sn solution in the thin films | Film thickness (nm) |
|---|---|---|---|---|
| S1 | 1,000 | 0 | 0 | 192 |
| S2 | 800 | 200 | 20 | 201 |
| S3 | 600 | 400 | 40 | 195 |
| S4 | 400 | 600 | 60 | 198 |
| S5 | 200 | 800 | 80 | 204 |
| S6 | 0 | 1,000 | 100 | 190 |

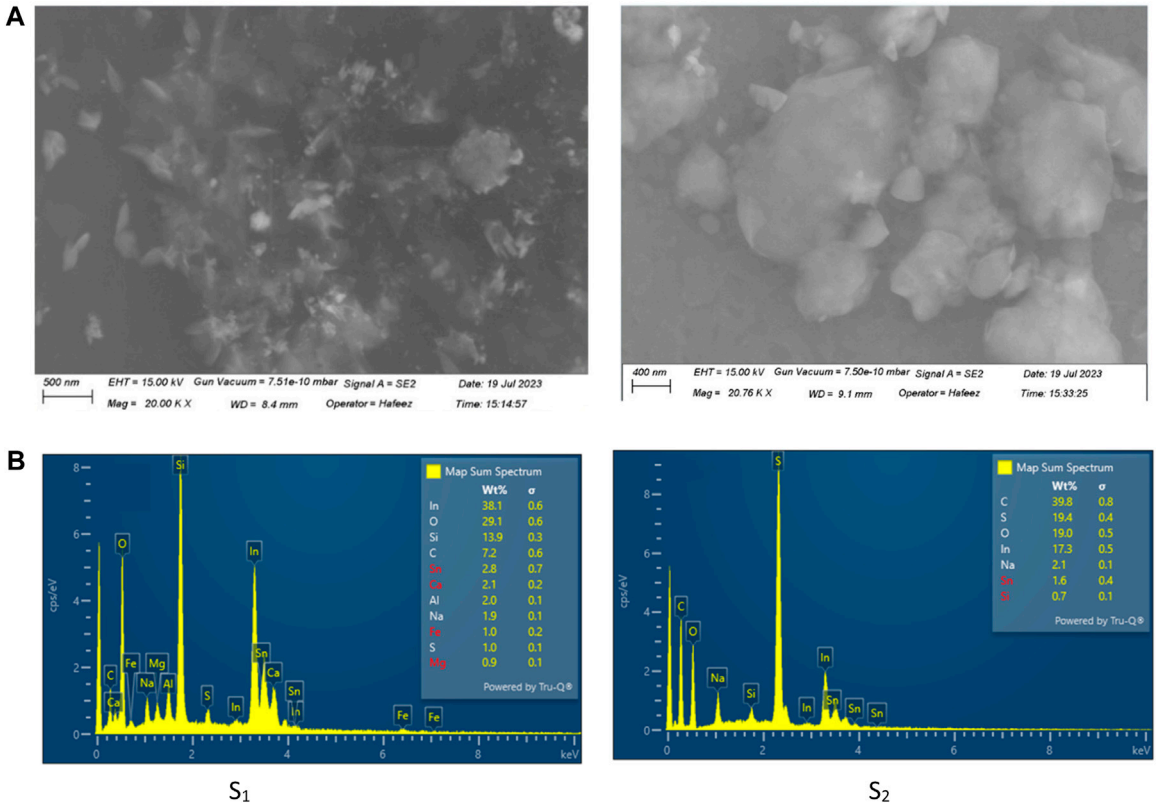


FIGURE 1
**(A)** SEM images and **(B)** EDS mapping and elemental distribution for S2 and S3 samples.

## 2.3 Fabrication of PEDOT:PSS/Sn thin films on glass substrates

After the generation of Sn NPs inside the PEDOT:PSS solution (representing a precursor solution), different amounts or volume ratios from the precursor PEDOT:PSS solution containing Sn NPs were added to the pristine PEDOT:PSS solution. Therefore, different concentrations of Sn NPs are incorporated inside the PEDOT:PSS solution, as demonstrated in Table 1. Glass substrates having an area of 1 × 1 $cm^2$ were ultrasonically cleaned, washed with deionized water, dried in flowing nitrogen, and then, heated in a furnace at a temperature of 373 K for 10 min. Via oxygen plasma treatment, the cleaned glass substrates were treated at 60 W for 20 min at an air-flow rate of 0.5 mbar $s^{-1}$. Then, the PEDOT:PSS solution without and with different concentrations of Sn NPs was spin coated at 3,000 rpm onto cleaned and treated glass substrates following thermal annealing using a digitally controlled hot plate at 393 K for 10 min in an ambient atmosphere.

## 2.4 Measurements

The PEDOT:PSS films (~200 nm thickness) onto glass substrates without and with different concentrations of Sn NPs

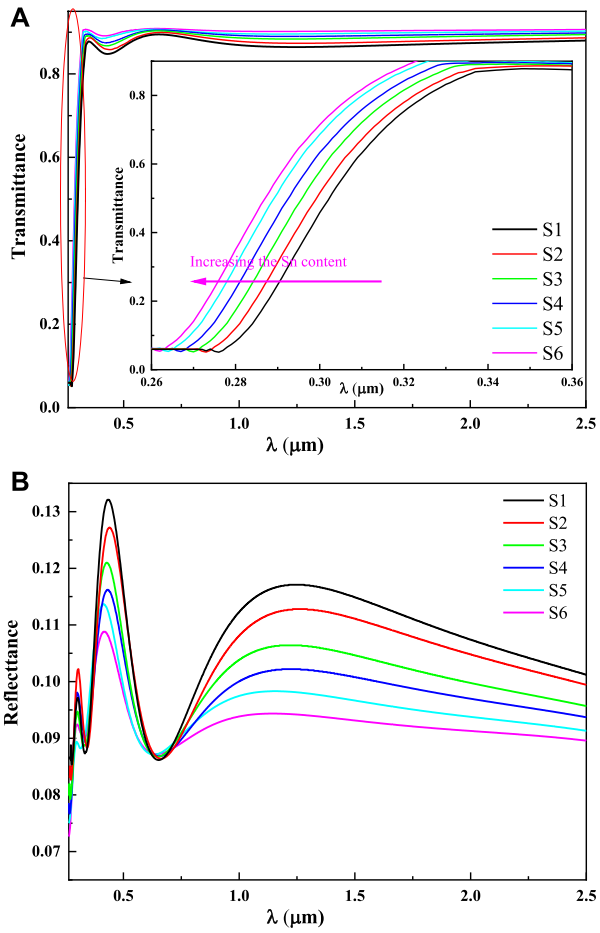


FIGURE 2
**(A)** T vs. λ and **(B)** R vs. λ for S1–S6 films.

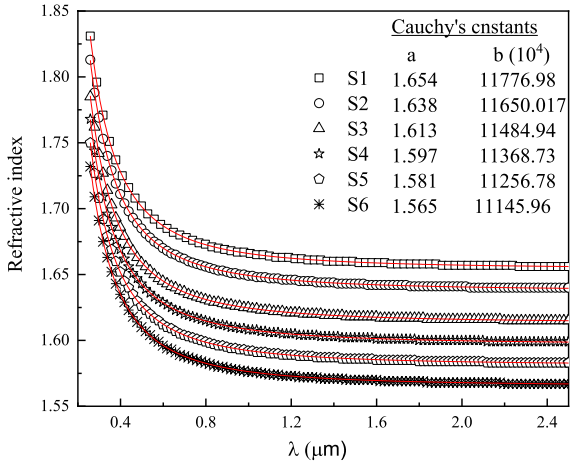


FIGURE 3
*n* vs. λ for S1–S6 films.

were characterized using a Horiba spectroscopic ellipsometer (model Smart-SE, USA) by measuring the refractive index and the extinction coefficient by investigating the film thickness. Furthermore, the films thicknesses were assured using Tolansky's interferometric technique [29]. The film transmittance and reflectance were measured in the 0.2–2.5 μm wavelength range using a Jasco-630 V double-beam spectrometer. The resistivity and sheet resistance of the PEDOT:PSS films with and without Sn NPs were measured by the Hall Effect setup at room temperature using a system from MMR technologies Inc. including the digital Hall Effect controller H5000 and digital temperature controller K2000.

## 3 Results and discussion

The shape of Sn nanoparticles, which were generated in the PEDOT:PSS solution, can be illustrated through SEM images, as shown in Figure 1 for samples numbers 2 and 3. From the SEM images of PEDOT:PSS/Sn films, it can be observed that Sn NPs are just physically suspended and spread over the PEDOT:PSS film, without interaction (chemically) with the matrix of the PEDOT:PSS film. Figure 1 shows that Sn NPs can be generated in the PEDOT:PSS solution with varying sizes influenced by ultrasonic power and the acidic nature of the PEDOT:PSS solution. Moreover, sizable Sn pieces are observable in the PEDOT:PSS/Sn films. From the SEM images of the Sn NPs embedded in PEDOT:PSS films in Figure 1 for samples S2 and S3, it appears that there is a wide distribution in NP sizes.

Figure 2 shows the $T(\lambda)$ and $R(\lambda)$ for the films under study. The inset of Figure 2A shows the region of strong absorption. Sample S1 has the lowest $T$ values and the largest $R$ values, which are normally for the changes of $T$ and $R$ with $\lambda$. From this figure, it can be seen that there is a clear blueshift with the addition of Sn content. The variation of $T$ values with $\lambda$ is opposite to the change in $R$ values. Furthermore, the film with low transmittance has the largest optical density. Figure 2 shows the $T(\lambda)$ and $R(\lambda)$ for the films under study. The inset of Figure 2A shows the region of strong absorption. Sample S1 has the lowest $T$ values and the largest $R$ values, which are normally for the changes of $T$ and $R$ with $\lambda$. From this figure, there is a clear blueshift with the addition of Sn content. The variation of $T$ values with $\lambda$ is opposite to the change in $R$ values. Furthermore, the film with low transmittance has the largest optical density. Within the 0.4–2.5 μm spectral range, the sum of the transmittance, T, and reflectance, R, is almost equal to unity and there is neither absorbed, A, nor scattered, S, electromagnetic (EM) waves, where T + R + A+ S = 1. This confirmed that the films under study have a good homogeneity and smooth surface [30, 31]. Furthermore, the optical transmittance (T) assured the ratio of light transmitted through a clear optical material. Many applications, such as optical fiber connections, optoelectronic sensors, and photonics, required that the film used should have a large transmittance. The transmittance spectrum of the film sample is affected by the preparation method and conditions, the thickness of the film, the film material itself, and the used substrate. For semiconducting films, the glazing film transmittance changes between 90% of the films of highest transparency to approximately 40% of highly coated materials. This range is affected by the film sample and its substrate [32]. The index of refraction ($n$) and the extinction parameter ($k$) of the

10.3389/fphy.2024.1331133

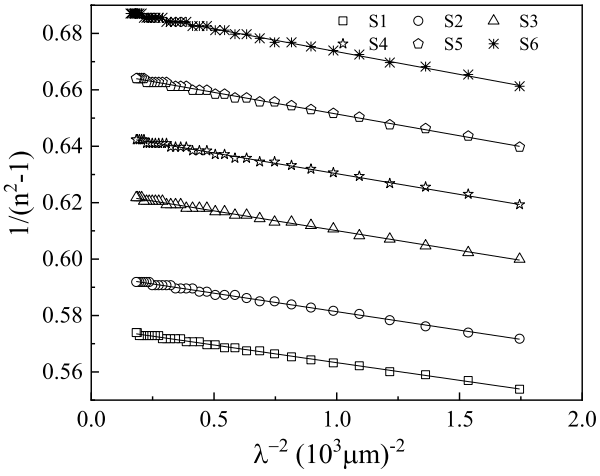


FIGURE 4
Slimmer's figure for S1–S6 films.

films were controlled by minimizing the errors $\Delta R(\lambda) = R_{exp}(\lambda) - R_{cal}(\lambda)$, $\Delta T(\lambda) = T_{exp}(\lambda) - T_{cal}(\lambda)$ using Murman's exact equations [33–35]. Figure 3 shows the $n$ values as a function of $\lambda$. The $n$ values decrease as Sn amounts increase, which would be expected due to the decrease in film reflectivity. Furthermore, the $n$ values decrease with the increase in $\lambda$, which is normal dispersion according to Cauchy's relationship [36].

$$n(\lambda) = a + \frac{b}{\lambda^2}, \tag{1}$$

where constants a and b are given in the same figure. The stationary or static refractive index ($(n(\lambda\ddot{\infty}\infty))$) may be calculated by substituting $\lambda = \infty$ in relationship (1). Then, Eq. (1) tends to $n(\infty) = a$.

## 3.1 Dispersion parameters

According to the simple dispersion model suggested by Sellmeier, in the low absorption range, the index of refraction $n$ of a dielectric medium can be written as follows [37]:

$$n^2 - 1 = \frac{s_o\lambda_o^2}{1 - (\lambda_o/\lambda)^2}, \tag{2}$$

where $\lambda_o$ and $S_o$ are the mean oscillator position and mean oscillator strength, respectively. The above equation can be rearranged as

$$\frac{1}{n^2 - 1} = \frac{1}{s_o\lambda_o^2} - \frac{1}{s_o}\left(\frac{1}{\lambda^2}\right). \tag{3}$$

Both $\lambda_o$ and $S_o$ values can be obtained from the slope ($S_o^{-1}$) and intersect ($1/s_o\lambda_o^2$) of the plots of $(n^2 - 1)^{-1}$ *versus* $\lambda^2$, as shown in Figure 4. The blueshift in transmittance spectra (Figure 2A) was assured by the decrease in $\lambda_o$ values with the increase in Sn concentrations. On the other side, the $S_o$ values decreased with the increase in Sn concentrations, which confirmed the validity of relationship (3). It is well known that the energy ($E$) and wavelength ($\lambda$ ) were correlated through this relationship

TABLE 2 Optical constants for different Sn NP concentrations incorporated into the PEDOT:PSS solution.

| Sample | $E_d$ | $E_o$ | $E_g^{in}$ | $E_g^d$ | $E_e$ | $M_{-1}$ | $M_{-3}$ | $n_o$ | $\varepsilon_L$ | $E_g/E_0$ | $\lambda_o$ | S ($10^{13}$) | $B^{0.5}$ | $W_p$ | N/m* | χ(3) | n2 |
|---|---|---|---|---|---|---|---|---|---|---|---|---|---|---|---|---|---|
| | eV | | | | | | | | | | nm | $m^{-2}$ | $\sqrt{cm.eV}$ | $10^{14}$Hz | $10^{54}kg^{-1}m^{-3}$ | $10^{-13}$ esu | $10^{-12}$esu |
| S1 | 14.61 | 8.11 | 3.08 | 3.97 | 0.6890 | 5.975 | 0.091 | 1.67 | 2.80 | 2.64 | 153 | 7.67 | 331 | 2.396 | 4.42 | 4.23 | 9.52 |
| S2 | 14.05 | 8.17 | 3.12 | 3.99 | 0.6734 | 5.823 | 0.087 | 1.65 | 2.72 | 2.62 | 152 | 7.43 | 336 | 2.386 | 4.25 | 3.52 | 8.04 |
| S3 | 13.25 | 8.22 | 3.15 | 4.06 | 0.6690 | 5.601 | 0.083 | 1.62 | 2.61 | 2.61 | 151 | 7.05 | 339 | 2.410 | 4.17 | 2.72 | 6.34 |
| S4 | 12.74 | 8.27 | 3.19 | 4.09 | 0.6640 | 5.455 | 0.080 | 1.59 | 2.54 | 2.60 | 150 | 6.82 | 342 | 2.401 | 4.02 | 2.27 | 5.36 |
| S5 | 12.25 | 8.35 | 3.23 | 4.14 | 0.6567 | 5.315 | 0.076 | 1.57 | 2.47 | 2.59 | 149 | 6.62 | 347 | 2.391 | 3.87 | 1.86 | 4.47 |
| S6 | 11.76 | 8.41 | 3.27 | 4.17 | 0.6396 | 5.172 | 0.073 | 1.55 | 2.40 | 2.57 | 148 | 6.40 | 352 | 2.398 | 3.79 | 1.54 | 3.74 |

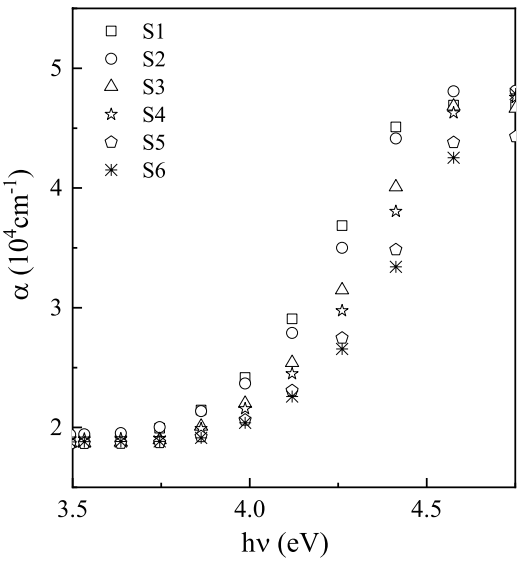


FIGURE 5
α vs. hν for S1–S6 films.

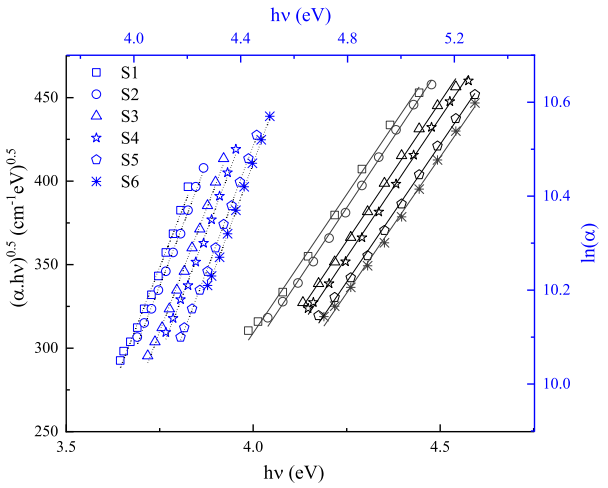


FIGURE 6
$(\alpha h\nu)^{0.5}$ and ln(α) vs. *hν* for S1–S6 films.

($E = hc/\lambda$, where both $h$ and $c$ have the same meaning here [38]). Therefore, the energy of a single oscillator ($E_o$) for GSAT films is determined with the help of $\lambda_o$ values using the following equation: ($E_o = hc/\lambda_o$). Tanaka [39] stated that the $E_g$ value for non-direct transition scales is $E_o/2 \approx E_g$ (Table 1). When $\lambda \vec{x} \infty$, i.e., $h\nu \vec{x} 0.0$, the above equation tends to $n_o^2 - 1 = s_o\lambda_o^2$; then, the value of the static index of refraction $n(\infty)$ or $n_o$ is given by $n_o = \sqrt{s_o\lambda_o^2 + 1}$. The estimated values of $n_o$ are the same as those determined from Cauchy's relationship (Figure 3). Sharda et al. [40] found a correlation between the oscillator energy of dispersion ($E_d$) and oscillator strength ($S_o$) which can be written in the form ($E_d = S_o(hc)^2/E_o$). The $E_d$ values are decreased with the increase in Sn concentrations. The $E_d$ value is directly affected by the operative coordination number of the cation adjacent to the anion ($N_c$), the anion official chemical valency ($Z_a$), and the valence electrons/anion active number ($N_e$). Therefore, $E_d$ was represented as $E_d = \beta N_c Z_a N_e$ ($eV$), where $\beta = 0.26 \pm 0.03\,eV$ and $0.37 \pm 0.04\,eV$ for ionic and covalent, respectively. There are two important parameters, namely, the plasma frequency ($\omega_p$) and the free carriers ($N$)/active mass ($m^*$) ratio, which can be evaluated with the help of $E_g$ through the following relationships [41]:

$$(n(0))^2 = 1 + \left(\hbar\omega_p / E_g\right)^2, \tag{4}$$

$$\omega_p^2 = (4\pi/\varepsilon_0)e^2(N/m^*). \tag{5}$$

The evaluated $\omega_p^2$ and $N/m^*$ values are shown in Table 2. According to Eqs (4, 5), both $\omega_p$ and $N/m^*$ values as well as the $n_o$ value behave, which is consistent with the above relations. Considering $m^* = 0.4m_e$, the free carrier's concentrations were estimated (Table 2). The $N$ values decreased with the increase in Sn contents, which is consistent with the observed increase in the $E_g$ value.

The optical moments, $M_{-1}$ and $M_{-3}$, stand for the responsivity of the dielectric sample and the usual bond ferocity. By utilizing the WDD model and the following relationship, one can estimate these moments as follows [42]:

$$E_0^2 = \frac{M_{-1}}{M_{-3}} \text{ and } E_d^2 = \frac{M_{-1}^3}{M_{-3}}. \tag{6}$$

We can compute $M_{-1}$ and $M_{-3}$ as follows:

$$M_{-1} = \frac{E_d}{E_0} \text{ and } M_{-3} = \frac{M_{-1}}{E_0^2}. \tag{7}$$

The estimated values of $M_{-1}$ are significantly higher than those of $M_{-3}$ ($M_{-1} \gg M_{-3}$), and they decrease as the concentration of Sn increases. The decreased $M_{-1}$ and $M_{-3}$ values in the films are strongly associated with this reduced polarization caused by the addition of Sn elements and an increase in composition. It is noteworthy that several parameters, such as the dielectric constant, valence electrons, film thickness, and annealing temperature, can affect these moments in the films [42, 43].

### 3.1.1 Absorbance coefficient and optical band gap

The excellence and evidence of thin films, including their concentrations, surface properties, and suitability, are demonstrated by the absorbance value ($x_a$). This value is interrelated with the absorption coefficient ($\alpha$) using the equation ($x_a = exp(-4\pi k\bar{t}/\lambda) = exp(-\alpha\bar{t})$). With the help of $k$ values, the $\alpha$ values have been estimated for the films under study ($\alpha = 4\pi k/\lambda$). The $\alpha$ changes due to the incident photon energy ($h\nu$) are shown in Figure 5. From this figure, it was noted that the $\alpha$ values increased with the increase in $h\nu$; however, the absorption edge shifted toward the higher energies with the enhancement of *Sn* contents, which means an increase in the optical band gap of the films. When choosing a semiconductor material for potential work, the energy of the optical band gap ($E_g$) plays a fundamental role. According to Tauc's correlation of the accepted indirect transitions, the energy dependence of $E_g$ is expressed as [44, 45]

$$\alpha h\nu = B\left(h\nu - E_g^{exp}\right)^m, \tag{8}$$

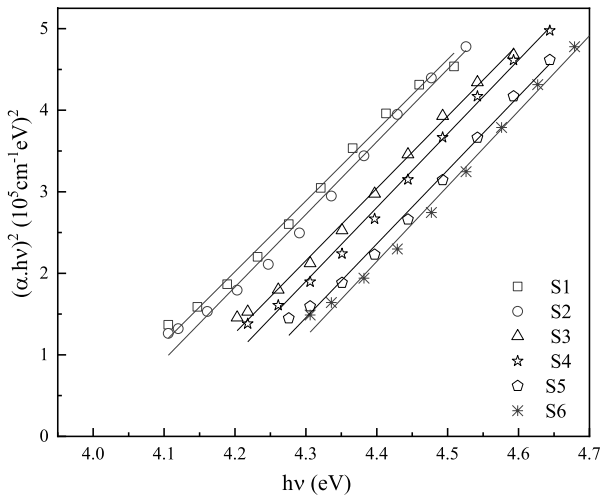


FIGURE 7
$(\alpha h\nu)^2$ and ln(α) vs. hν for S1–S6 films.

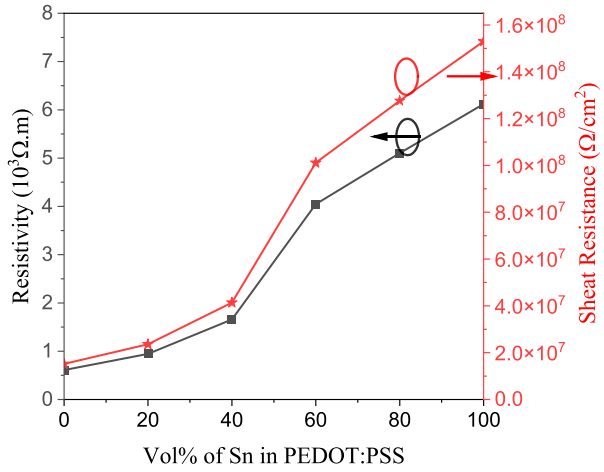


FIGURE 8
Resistivity and sheet resistance vs. Sn contents for S1–S6 films.

where $B$ represents the band tail parameter and $m$ = 2.0 and 0.5 for allowed non-direct and direct transitions, respectively. According to Tauc, crystalline materials show authorized direct transitions, while amorphous materials show permissible indirect transitions. The $E_g$ values are evaluated by extrapolation $(\alpha h\nu)^{0.5}$ẋ0.0 (Figure 6) and listed in Table 2 as $E_g^{ind}$. Furthermore, the $B^{0.5}$ values are shown in Table 2 and are found to increase with the increase in the concentrations of *Sn*. This behavior of $E_g$ is because of the observed clear blueshift of the absorption edge. $E_g^{ind}$ is indirectly related to the disorders and the localized state width [45]. As a result, the increase in the values of $E_g^{ind}$ reflects the increase of disorders in PEDOT:PSS/Sn films as the Sn at% contents are added to the films; consequentially, tail states in the gap are shrunk, which was confirmed by the increase in $B^{0.5}$ values. The $B^{0.5}$ parameter is directly proportional to the $E_g^{ind}$ values (see Table 2), while it is inversely proportional to the width of localized states ($E_e$). According to the Davis and Mott model (DMM), the $B$ parameter can be expressed as [46]

$$B = \sigma_{min} / n\varepsilon_o c E_e, \tag{9}$$

where n represents the film's refractive index, $\sigma_{min}$ represents the lowest metallic conductivity, and $\varepsilon_o$ and $c$ have the same meaning and values here [38, 47]. On the other side, Figure 7 represents the plots of $(\alpha h\nu)^2$ vs. $h\nu$ for the films under study. The best fit confirms the allowed direct transitions and successfully describes the absorption mechanism in these films. The $E_g^{dir}$ values are higher than those of $E_g^{ind}$ and increased with the increase in the concentrations of Sn. The results are found to be in excellent agreement with electrical measurements (Figure 8). Figure 8 shows the measured resistivity and sheet resistance of the samples under study. Both the resistivity and sheet resistance increase with the increase in Sn contents. Figure 8 shows both the resistivity and sheet resistance of the PEDOT:PSS/Sn films increase as the concentration of Sn NPs increases. This trend could be attributed to the likelihood of a reduction in film thickness with an increase in the concentration of Sn NPs in the films. This reduction may occur due to the centrifugal force applied to the large pieces of Sn microstructures immersed in the PEDOT:PSS solution, as evident in the SEM images of PEDOT:PSS films containing Sn microstructures shown in Figure 1. The centrifugal force applied to the large pieces of Sn microstructures can displace a portion of the PEDOT:PSS solution beyond the glass substrate during the spin coating process. Consequently, the thickness of PEDOT:PSS films may decrease with an increase in the concentration of the larger Sn microstructures. The decrease in PEDOT:PSS/Sn film thickness tends to decrease the resistivity and sheet resistance of PEDOT:PSS/Sn films. As a result, the thickness of PEDOT:PSS films may decrease with an increase in the concentration of the larger Sn microstructures. Therefore, this reduction in the thickness of PEDOT:PSS/Sn films tends to decrease the resistivity and sheet resistance. The absorption spectra show essential information interpreting the semiconductor composition and $E_g$. Three major categories characterize the absorption spectra of any semiconductor: The first region is the weak absorption, which is due to defects and impurities; the second is the region which is due to structure- and system-order agitations; finally, there is the strong absorption, and it investigates $E_g$.

In the region of low absorption, the absorption coefficient shows an exponential dependence on photon energy, $h\nu$, according to Urbach's relationship [48].

$$ln(\alpha) = ln(\alpha_0) + \frac{h\nu}{E_e}, \tag{10}$$

where $\alpha_0$ is a constant and $E_e$ signifies the Urbach's energy representative, the localized state width. The exponential part of $\alpha$, which is closer to the absorption edge, is known as the Urbach tail, and $E_e$ also identifies the disorder degree in the material. $E_e$ values are calculated as the slope$^{-1}$ of the straight lines in Figure 7, whereas the intersect investigates $\ln(\alpha_0)$. The $E_e$ values are listed in Table 2. The $E_e$ values are decreased when the Sn content in the films is increased. Similar behavior has been associated with a significant increase in bond strength due to the decrease in defect state density and disorderliness degree.

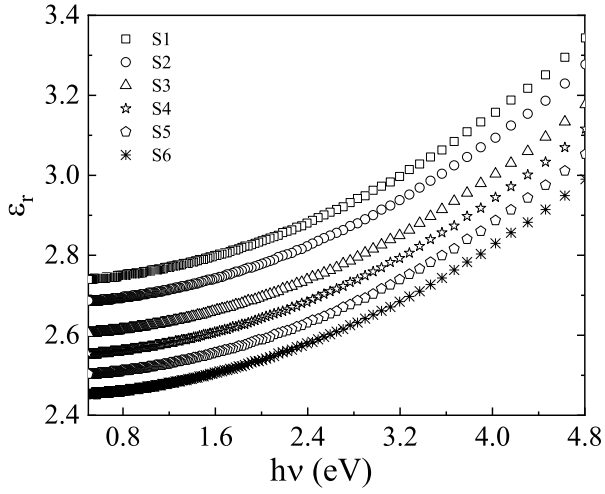


FIGURE 9
$\varepsilon_r$ vs. $h\nu$ for S1–S6 films.

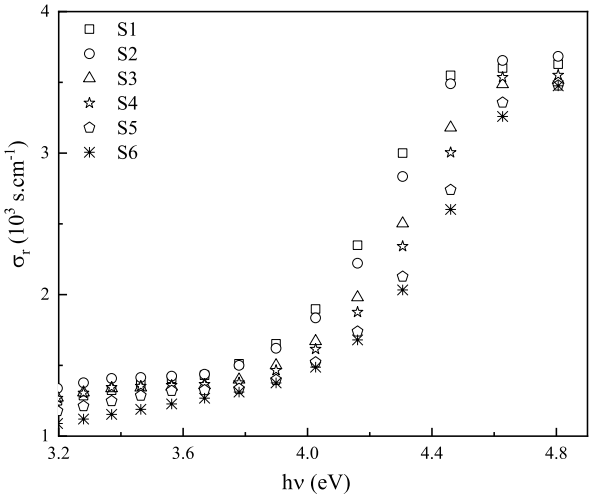


FIGURE 11
$\sigma_r$ vs. $h\nu$ for S1–S6 films.

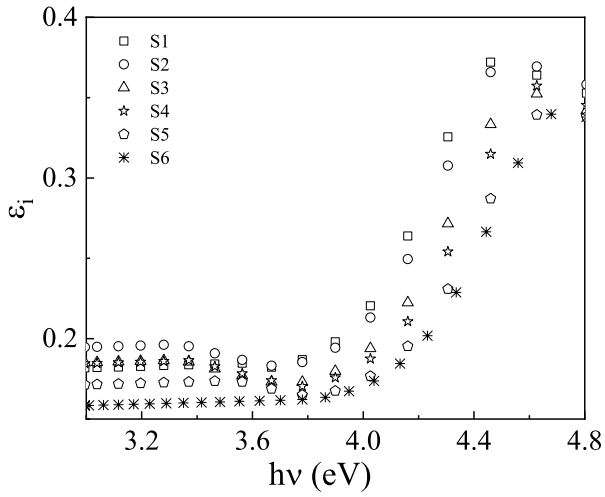


FIGURE 10
$\varepsilon_i$ vs. $h\nu$ for S1–S6 films.

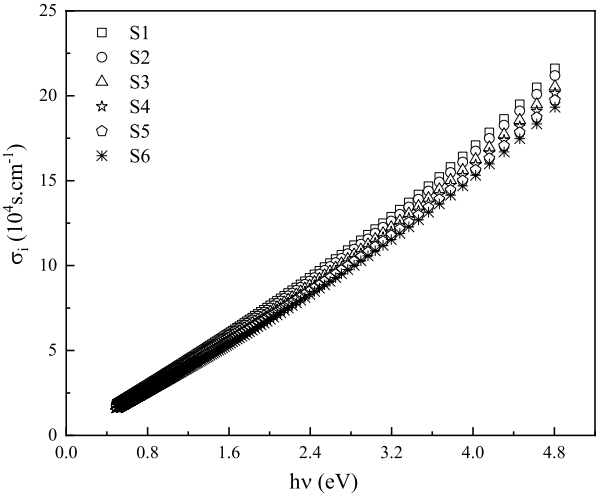


FIGURE 12
$\sigma_i$ vs. $h\nu$ for S1–S6 films.

### 3.1.2 Dielectric optical constants

When determining whether a material is suitable for optoelectronic devices, the dielectric constant is a key consideration [31, 49]. The polarizability of materials and the dielectric constant are correlated in the optical domain. The values of the energy loss function, polarizabilities, dissipation parameter, and dielectric loss are only a few examples of variables whose information is usefully provided by the dielectric constant. Both the real and imaginary parts ($\varepsilon_r$ and $\varepsilon_i$, respectively) constitute the complex dielectric constant $\varepsilon^*$, and these parts are correlated by the following relationship [38]:

$$\varepsilon^* = \varepsilon_r + i\varepsilon_i. \tag{11}$$

The real part, $\varepsilon_r$, has a substantial impact on how EM waves disperse as they move through a sample, slowing down the speed of light. The $\varepsilon_i$ component, which results from the motion of the dipole, is what distinguishes the dielectric's absorption of energy from the alternating electric field [31]. The following relationships establish a direct connection between $n$, $k$, $\varepsilon_r$, and $\varepsilon_i$ [38]:

$$\varepsilon_r = n^2 - k^2, \tag{12}$$

$$\varepsilon_i = 2nk. \tag{13}$$

Figures 9, 10 show how $\varepsilon_r$ *and* $\varepsilon_i$ react to the energy of EM waves that are incident on them. The values of $\varepsilon_r$ demonstrate a tendency like the refractive index ($n$) and are much greater than $\varepsilon_i$, whereas $\varepsilon_i$ exhibits a pattern like the extinction parameter ($k$). With the increase in Sn amounts in the current films, both components of the dielectric constant decreased. Higher Sn concentrations in these films cause EM waves to flow more slowly, which increases EM wave dispersion and absorption

within the system. As a result, the optical conductivity decreases [39, 43, 50, 51]. The above equation tends to $\varepsilon_{\infty} = n^2$ for the range of transparency. The $\varepsilon_{\infty}$ values of PEDOT:PSS/Sn films decrease with the increase in Sn contents. It has been demonstrated that the most direct and efficient way to increase the transmission speed and efficiency of microelectronic devices and to encourage the development of high-frequency and high-speed elastic circuit boards is to decrease the dielectric constant of insulating dielectric materials used in circuit boards [52]. For dielectric materials, the optical conductivity is typically low and correlates with the dielectric loss. Optical conductivity provides a connection between the induced current density in semiconductor materials and the electric field amplitude generated at various frequencies. This linear response function represents the conductivity of electric fields, which is commonly considered static or time-independent [53].

Complex optical conductivity ($\sigma^{*}_{op}$), which is associated with the glass complex dielectric constant through the formulas, affects the optical response of the material that interacts with photon energy [38].

$$\sigma^{*}_{op} = \sigma_r(\omega) + i\,\sigma_i(\omega). \tag{14}$$

The imaginary portion of optical conductivity, $\sigma_i(\omega)$, is represented as $\sigma_i(\omega) = \omega\varepsilon_o\varepsilon_r$ [38], where $\varepsilon_0$ denotes the free space permittivity. The real portion of optical conductivity, $\sigma_r(\omega)$, is supplied by $\sigma_r(\omega) = \omega\varepsilon_o\varepsilon_r$. Figures 11, 12 show how optical conductivity responds to various GSAT films. $\sigma_i(\omega)$ values are noticeably greater than the actual ones, as anticipated ($\varepsilon_r \gg \varepsilon_i$). These results are consistent with those previously published [54–56]. At higher energies, the values of $\sigma_r$ and $\sigma_i$ are incredibly significant, but at lower energies, they tend to approach 0.

## 3.2 Optical nonlinearity

The electric field effect on the nonlinear refractive index is linked to the high-order susceptibility and may be written as $n = n_0 + n_2\langle E^2\rangle$, where $n_2$ represents the nonlinear index of refraction and it is not affected by the incident photon intensity, $n_0 \gg n_2$, and $\langle E^2\rangle$ represents the electric field mean square of the optical sub-beam [57]. The polarity and electric field underneath the intense electric field of the strong light beam are taken as scalars, forming a power series as follows [58]:

$$P = \chi^{(1)}E + \chi^{(2)}E^2 + \chi^{(3)}E^3 + \ldots, \tag{15}$$

where $\chi^{(1)}$ shows the established linear retort and $\chi^{(2)}$ and $\chi^{(3)}$ correspond to the second- and third-order nonlinear susceptibilities, respectively. $n_2$ relates to $\chi^{(3)}$, while the value of $\chi^{(2)}$ is 0 for glass, liquid, and gas. $\chi^{(3)}$ for glasses, to think about the smallest nonlinear order, is generated by inflammations in the translucent frequency range well below the optical band gap. In CGS films, the values of $\chi^{(3)}$ and $n_2$ are estimated by using the semiempirical relationship as follows [59]:

$$\chi^{(3)} = 1.7\,x\,10^{-10}\left[\frac{n_0^2 - 1}{4}\right]^4, \tag{16}$$

$$n_2 = \frac{12\pi\chi^{(3)}}{n_0}. \tag{17}$$

The calculated values of $\chi^{(3)}$ and $n_2$ are listed in Table 2. All the nonlinear values decrease with Sn contents. The source of nonlinearity is presumed to be the electronic benevolence of films. The $\chi^{(3)}$ and $n_2$ values are affected by the linear optical parameters. Both $\chi^{(3)}$ and $n_2$ values are inversely proportional to the $E_g$ value. The high nonlinearity of the film is related to the structural unit's flexibility. Such films can be used in all optical switching, optical limiting, optical phase modulation, and frequency conversion [60, 61].

# 4 Conclusion

The incorporation of Sn NPs inside PEDOT:PSS thin films was successfully performed through an innovative ultrasonic ablation technique. Using the measured film transmission and reflection spectra, the refractive index ($n$) and extinction coefficient ($k$) were carefully estimated. With the increase in Sn amounts, the n values decreased, while the optical band gap ($E_g$) values increased. The increase in the optical band gap of the PEDOT:PSS buffer layer in solar cell applications is expected to enhance the performance parameters of solar cells. The increase in the optical band gap of the PEDOT:PSS buffer layer can improve the blocking of photoelectrons toward the solar cell anode. Consequently, it helps prevent their recombination with holes at the solar cell anode. The behavior of n changes with the wavelength, as described by the Cauchy's relationship. The $n$ and $k$ values are the keys to a complete estimation of the optical, dielectric, and nonlinear parameters. Sellmeier's dispersion model helps us estimate the dispersion parameters. The dielectric constant of PEDOT:PSS/Sn films is reduced with the increase in Sn contents, which directly improves the transmittance speed and efficacy of microelectronic devices and promotes the development of large-frequency and high-speed elastic circuit boards. The high values of nonlinear optical constants make the present films suitable for all optical devices and organic solar cells.

# Data availability statement

The raw data supporting the conclusions of this article will be made available by the authors, without undue reservation.

# Author contributions

KA: methodology, resources, software, and writing–original draft. YI: data curation, funding acquisition, project administration, and writing–review and editing. ZS: conceptualization, formal analysis, investigation, visualization, and writing–original draft. TA: investigation, resources, supervision, and writing–original draft. AA: formal analysis, methodology, software, and writing–original draft. SG: formal

analysis, investigation, resources, validation, and writing–review and editing. HA: conceptualization, supervision, validation, visualization, and writing–review and editing. MI: investigation, supervision, visualization, and writing–review and editing.

## Funding

The authors declare that financial support was received for the research, authorship, and/or publication of this article. This work was financially supported by the Deanship of Scientific Research in the Islamic University of Madinah, Saudi Arabia [The Research Groups Grant (First Call): Number 945].

## Conflict of interest

The authors declare that the research was conducted in the absence of any commercial or financial relationships that could be construed as a potential conflict of interest.

## Publisher's note



## References

1. Zhu Z, Liu C, Jiang F, Xu J, Liu E. Effective treatment methods on PEDOT:PSS to enhance its thermoelectric performance. *Synth Met* (2017) 225:31–40. doi:10.1016/j.synthmet.2016.11.011

2. Kim G-E, Shin D-K, Lee J-Y, Park J. Effect of surface morphology of slot-die heads on roll-to-roll coatings of fine PEDOT:PSS stripes. *Org Elect* (2019) 66:116–25. doi:10.1016/j.orgel.2018.12.033

3. Koidis C, Logothetidis S, Kapnopoulos C, Karagiannidis PG, Laskarakis A, Hastas NA. Substrate treatment and drying conditions effect on the properties of roll-to-roll gravure printed PEDOT:PSS thin films. *Mater Sci Eng B* (2011) 176:1556–61. doi:10.1016/j.mseb.2011.03.007

4. Griffin J, Ryan AJ, Lidzey DG. Solution modification of PEDOT:PSS inks for ultrasonic spray coating. *Org Elect* (2017) 41:245–50. doi:10.1016/j.orgel.2016.11.011

5. Kim B-J, Han S-H, Park J-S. Properties of CNTs coated by PEDOT:PSS films via spin-coating and electrophoretic deposition methods for flexible transparent electrodes. *Surf Coat Tech* (2015) 271:22–6. doi:10.1016/j.surfcoat.2015.01.045

6. Zabihi F, Xie Y, Gao S, Eslamian M. Morphology, conductivity, and wetting characteristics of PEDOT:PSS thin films deposited by spin and spray coating. *Appl Surf Sci* (2015) 338:163–77. doi:10.1016/j.apsusc.2015.02.128

7. Arora S, Singh V, Arora M, Pal Tandon R. Evaluating effect of surface state density at the interfaces in degraded bulk heterojunction organic solar cell. *Physica B: Condensed Matter* (2012) 407:3044–6. doi:10.1016/j.physb.2011.08.086

8. Singh V, Arora S, Arora M, Sharma V, Tandon RP. Characterization of doped PEDOT: PSS and its influence on the performance and degradation of organic solar cells. *Semiconductor Sci Tech* (2014) 29. doi:10.1088/0268-1242/29/4/045020

9. Sun K, Zhang S, Li P, Xia Y, Zhang X, Du D, et al. Review on application of PEDOTs and PEDOT:PSS in energy conversion and storage devices. *J Mater Sci Mater Elect* (2015) 26:4438–62. doi:10.1007/s10854-015-2895-5

10. Lee JH, Jung JP, Jang E, Lee KB, Hwang YJ, Min BK, et al. PEDOT-PSS embedded comb copolymer membranes with improved CO2 capture. *J Membr Sci* (2016) 518:21–30. doi:10.1016/j.memsci.2016.06.025

11. Meng Y, Ahmadi M, Wu X, Xu T, Xu L, Xiong Z, et al. High performance and stable all-inorganic perovskite light emitting diodes by reducing luminescence quenching at PEDOT:PSS/Perovskites interface. *Org Elect* (2019) 64:47–53. doi:10.1016/j.orgel.2018.10.014

12. Meng Q, Jiang Q, Cai K, Chen L. Preparation and thermoelectric properties of PEDOT:PSS coated Te nanorod/PEDOT:PSS composite films. *Org Elect* (2019) 64:79–85. doi:10.1016/j.orgel.2018.10.010

13. Baruah B, Kumar A. PEDOT:PSS/$MnO_2$/rGO ternary nanocomposite based anode catalyst for enhanced electrocatalytic activity of methanol oxidation for direct methanol fuel cell. *Synth Met* (2018) 245:74–86. doi:10.1016/j.synthmet.2018.08.009

14. Singh SB, Kshetri T, Singh TI, Kim NH, Lee JH. Embedded PEDOT:PSS/AgNFs network flexible transparent electrode for solid-state supercapacitor. *Chem Eng J* (2019) 359:197–207. doi:10.1016/j.cej.2018.11.160

15. Sarker AK, Kim J, Wee B-H, Song H-J, Lee Y, Hong J-D, et al. Hydroiodic acid treated PEDOT:PSS thin film as transparent electrode: an approach towards ITO free organic photovoltaics. *RSC Adv* (2015) 5:52019–25. doi:10.1039/c5ra07136d

16. Alemu D, Wei H-Y, Ho K-C, Chu C-W. Highly conductive PEDOT:PSS electrode by simple film treatment with methanol for ITO-free polymer solar cells. *Energ Environ Sci* (2012) 5:9662–71. doi:10.1039/c2ee22595f

17. Kim JY, Jung JH, Lee DE, Joo J. Enhancement of electrical conductivity of poly(3,4-ethylenedioxythiophene)/poly(4-styrenesulfonate) by a change of solvents. *Synth Met* (2002) 126:311–6. doi:10.1016/s0379-6779(01)00576-8

18. Huang J, Miller PF, Wilson JS, de Mello AJ, de Mello JC, Bradley DDC. Investigation of the effects of doping and post-deposition treatments on the conductivity, morphology, and work function of poly(3,4-ethylenedioxythiophene)/poly(styrene sulfonate) films. *Adv Funct Mater* (2005) 15:290–6. doi:10.1002/adfm.200400073

19. Zhou Y, Cheun H, Choi S, Potscavage WJ, Jr., Fuentes-Hernandez C, Kippelen B. Indium tin oxide-free and metal-free semitransparent organic solar cells. *Appl Phys Lett* (2010) 97:153304. doi:10.1063/1.3499299

20. Badre C, Marquant L, Alsayed AM, Hough LA. Highly conductive poly(3,4-ethylenedioxythiophene):poly (styrenesulfonate) films using 1-Ethyl-3-methylimidazolium tetracyanoborate ionic liquid. *Adv Funct Mater* (2012) 22:2723–7. doi:10.1002/adfm.201200225

21. Vosgueritchian M, Lipomi DJ, Bao Z. Highly conductive and transparent PEDOT:PSS films with a fluorosurfactant for stretchable and flexible transparent electrodes. *Adv Funct Mater* (2012) 22:421–8. doi:10.1002/adfm.201101775

22. Ko C-J, Lin Y-K, Chen F-C, Chu C-W. Modified buffer layers for polymer photovoltaic devices. *Appl Phys Lett* (2007) 90:063509. doi:10.1063/1.2437703

23. Lee I, Lee S, Kim H, LeeKim HY. Polymer solar cells with polymer/carbon nanotube composite hole-collecting buffer layers. *Open Phys Chem J* (2010) 4:1–3. doi:10.2174/1874067701004010001

24. Notarianni M, Vernon K, Chou A, Aljada M, Liu J, Motta N. Plasmonic effect of gold nanoparticles in organic solar cells. *Solar Energy* (2014) 106:23–37. doi:10.1016/j.solener.2013.09.026

25. Woo S, Jeong JH, Lyu HK, Han YS, Kim Y. *In situ*-prepared composite materials of PEDOT: PSS buffer layer-metal nanoparticles and their application to organic solar cells. *Nanoscale Res Lett* (2012) 7:641. doi:10.1186/1556-276x-7-641

26. Ismail YAM, Kishi N, Soga T. Ultrasonic ablation as a novel technique for producing pure aluminium nanoparticles dispersed in different liquids for different applications. *Jpn J Appl Phys* (2015) 54:075002. doi:10.7567/jjap.54.075002

27. Ismail YAM, Kishi N, Soga T. Improvement of organic solar cells using aluminium microstructures prepared in PEDOT:PSS buffer layer by using ultrasonic ablation technique. *Thin Solid Films* (2016) 616:73–9. doi:10.1016/j.tsf.2016.08.001

28. Ismail YAM. Aluminium nanoparticles prepared by ultrasonic ablation technique inside the active layer of organic solar cell. *J Nano Res* (2018) 51:48–60. doi:10.4028/www.scientific.net/jnanor.51.48

29. Tolansky S, Omar M. Thin-film interferometric techniques for high-magnification topographical studies. *Nature* (1952) 170:81–2. doi:10.1038/170081b0

30. Hassanien AS, Akl AA. Influence of composition on optical and dispersion parameters of thermally evaporated non-crystalline $Cd_{50}S_{50-x}Se_x$ thin films. *J Alloys Comp* (2015) 648:280–90. doi:10.1016/j.jallcom.2015.06.231

31. Hassanien AS, Sharma I. Dielectric properties, Optoelectrical parameters and electronic polarizability of thermally evaporated a-Pb-Se-Ge thin films. *Physica B: Condensed Matter* (2021) 622:413330. doi:10.1016/j.physb.2021.413330

32. Hassanien AS, Sharma I, Aly KA. Linear and nonlinear optical studies of thermally evaporated chalcogenide a-Pb-Se-Ge thin films. *Physica B: Condensed Matter* (2021) 613:412985. doi:10.1016/j.physb.2021.412985

33. Murmann H. Der spektrale Verlauf der anomalen optischen Konstanten dünnen Silbers. *Z für Physik* (1936) 101:643–8. doi:10.1007/BF01349608

34. Heavens OS. *Optical properties of thin solid films*. New York.: Dover Publications. (1965).

35. Ibraheem AA, Aly KA. Optical and dispersion parameters of Ge-Zn-Se glassy films for VIS and FTIR Applications. *Physica Scripta* (2023) 98:015810. doi:10.1088/1402-4896/aca630

36. Aly KA, Afify N, Abousehlly AM, Abd Elnaeim AM. Optical band gap and refractive index dispersion parameters of In–Se–Te amorphous films. *J Non-Crystalline Sol* (2011) 357:2029–34. doi:10.1016/j.jnoncrysol.2011.02.032

37. DrDomenico M, Jr., Wemple SH. Oxygen-octahedra ferroelectrics. I. Theory of electro-optical and nonlinear optical effects. *J Appl Phys* (2003) 40:720–34. doi:10.1063/1.1657458

38. Aly KA. Comment on the relationship between electrical and optical conductivity used in several recent papers published in the journal of materials science: materials in electronics. *J Mater Sci Mater Elect* (2022) 33:2889–98. doi:10.1007/s10854-021-07496-9

39. Kumar A, Ali V, Kumar S, Husain M. Studies on conductivity and optical properties of poly(o-toluidine)-ferrous sulfate composites. *Int J Polym Anal Characterization* (2011) 16:298–306. doi:10.1080/1023666x.2011.587945

40. Sharda S, Sharma E, Aly KA, Dahshan A, Sharma P. High refractive index (Dy) doped (GeTe2)80(In2Te3)20 thin films for sub-THz and millimeter-wave applications. *Ceramics Int* (2021) 47:34501–7. doi:10.1016/j.ceramint.2021.08.364

41. Minkov D, Vateva E, Skordeva E, Arsova D, Nikiforova M. Optical properties of Ge-As-S thin films. *J Non-Crystalline Sol* (1987) 90:481–4. doi:10.1016/s0022-3093(87)80469-6

42. Rafea MA, Farag AAM, Roushdy N. Structural and optical characteristics of nano-sized structure of $Zn_{0.5}Cd_{0.5S}$ thin films prepared by dip-coating method. *J Alloys Comp* (2009) 485:660–6. doi:10.1016/j.jallcom.2009.06.048

43. Hassanien AS, Aly KA, Akl AA. Study of optical properties of thermally evaporated ZnSe thin films annealed at different pulsed laser powers. *J Alloys Comp* (2016) 685:733–42. doi:10.1016/j.jallcom.2016.06.180

44. Hegazy HH, Dahshan A, Aly KA. Influence of Cu content on physical characterization and optical properties of new amorphous Ge–Se–Sb–Cu thin films. *Mater Res Express* (2019) 6:025204. doi:10.1088/2053-1591/aaee4b

45. Tauc J, Menth A. States in the gap. *J Non-Crystalline Sol* (1972) 8-10:569–85. doi:10.1016/0022-3093(72)90194-9

46. Davis EA, Mott NF. Conduction in non-crystalline systems V. Conductivity, optical absorption and photoconductivity in amorphous semiconductors. *Phil Mag A J Theor Exp Appl Phys* (1970) 22:0903–22. doi:10.1080/14786437008221061

47. Ibraheem AA, Aly KA. Physical characterization of Ge–Zn–Se thin films. *J Mater Sci Mater Elect* (2022) 33:26905–14. doi:10.1007/s10854-022-09355-7

48. Urbach F. The long-wavelength edge of photographic sensitivity and of the electronic absorption of solids. *Phys Rev* (1953) 92:1324. doi:10.1103/physrev.92.1324

49. Aly KA. Optical constants of quaternary Ge-As-Te-In amorphous thin films evaluated from their reflectance spectra. *Phil Mag* (2009) 89:1063–79. doi:10.1080/14786430902870542

50. Shen Q, Ayuzawa Y, Katayama K, Sawada T, Toyoda T. Separation of ultrafast photoexcited electron and hole dynamics in CdSe quantum dots adsorbed onto nanostructured TiO2 films. *Appl Phys Lett* (2010) 97:263113. doi:10.1063/1.3533374

51. Farag AAM, Yahia IS. Structural, absorption and optical dispersion characteristics of rhodamine B thin films prepared by drop casting technique. *Opt Commun* (2010) 283:4310–7. doi:10.1016/j.optcom.2010.06.081

52. Liu Y, Zhao X-Y, Sun Y-G, Li W-Z, Zhang X-S, Luan J. Synthesis and applications of low dielectric polyimide. *Resour Chemicals Mater* (2023) 2:49–62. doi:10.1016/j.recm.2022.08.001

53. Sharma I, Sharma P, Hassanien AS. Optical properties and optoelectrical parameters of the quaternary chalcogenide amorphous $Ge_{15}Sn_xS_{35-x}Te_{50}$ films. *J Non-Crystalline Sol* (2022) 590:121673. doi:10.1016/j.jnoncrysol.2022.121673

54. Sharda S, Sharma E, Aly KA, Dahshan A, Sharma P. Thermo-induced changes in the optical linearity and nonlinearity of Dy doped $(GeSe_2)_{80}(Sb_2Se_3)_{20}$ thin films. *Opt Quan Elect* (2022) 54:249. doi:10.1007/s11082-022-03653-4

55. Hassanien AS. Studies on dielectric properties, opto-electrical parameters and electronic polarizability of thermally evaporated amorphous $Cd_{50}S_{50-x}Se_x$ thin films. *J Alloys Comp* (2016) 671:566–78. doi:10.1016/j.jallcom.2016.02.126

56. El-Nahass MM, Farid AM, Atta AA. Structural and optical properties of Tris(8-hydroxyquinoline) aluminum (III) (Alq3) thermal evaporated thin films. *J Alloys Comp* (2010) 507:112–9. doi:10.1016/j.jallcom.2010.07.110

57. Tanaka K. Optical nonlinearity in photonic glasses. *J Mater Sci Mater Elect* (2005) 16:633–43. doi:10.1007/s10854-005-3738-6

58. Dimitrov V, Sakka S. Linear and nonlinear optical properties of simple oxides. II. *J Appl Phys* (1996) 79:1741–5. doi:10.1063/1.360963

59. Tichá H, Tichý L. Semiempirical relation between non-linear susceptibility (refractive index), linear refractive index and optical gap and its application to amorphous chalcogenides. *J Optoelectronics Adv Mater* (2002) 4:381–6.

60. Boyd RW. Chapter 6 - nonlinear Optics in the two-level approximation. In: Boyd RW, editor. *Nonlinear Optics*. 3rd ed. Burlington: Academic Press (2008). p. 277–328.

61. Agrawal GP. Preface. In: Agrawal GP, editor. *Applications of nonlinear fiber Optics*. 2nd ed. Burlington: Academic Press (2008). xiii-xiv.